An Investigation by AFM and TEM of the Mechanism of Anodic Formation of Nanoporosity in n-InP in KOH

C. O'Dwyer[†a], D. N. Buckley[†], D. Sutton[b], M. Serantoni and S. B. Newcomb[c]

Materials and Surface Science Institute, University of Limerick, Ireland

[†]Department of Physics, University of Limerick, Ireland

[a]*present address:* Tyndall National Institute, University College Cork, Ireland

[b]*present address:* Department of Applied Science, Limerick Institute of Technology, Ireland

[c]*present address:* Glebe Scientific Ltd., Glebe Laboratories, Newport, Co. Tipperary, Ireland

Abstract

The early stages of nanoporous layer formation, under anodic conditions in the absence of light, were investigated for n-type InP with a carrier concentration of ~3×10^{18} cm^{-3} in 5 mol dm^{-3} KOH and a mechanism for the process is proposed. At potentials less than ~0.35 V (SCE), spectroscopic ellipsometry and transmission electron microscopy (TEM) showed a thin oxide film on the surface. Atomic force micrography of electrode surfaces showed no pitting below ~0.35 V but clearly showed etch pit formation in the range 0.4 V to 0.53 V. The density of surface pits increased with time in both LPS and constant potential experiments, reaching a constant value at a time corresponding approximately to the current peak in linear sweep voltammograms and current-time curves at constant potential. TEM clearly showed individual nanoporous domains separated from the surface by a dense ~40 nm InP layer. It is concluded that each domain develops as a result of directionally preferential pore propagation from an individual surface pit which forms a channel through this near-surface layer. As they grow larger, domains meet and the merging of multiple domains eventually leads to a continuous nanoporous sub-surface region.

Introduction

Significant progress has been made in understanding the basic mechanisms for the formation of porous silicon under electrochemical conditions and several pore formation models have been proposed to account for the variety of pore types reported [1-3]. Pores that grow along the principal direction of current flow have been observed to lead to the formation of a porous layer in a relatively simple manner and the porosity is affected chiefly by the rate of nucleation of pores on the surface. However, crystallographically oriented pore growth, especially if the growth direction is not perpendicular to the equipotential surfaces in the sample, is comparatively more difficult to explain.

In comparison with silicon, only a limited number of investigations of the formation of porous III-V semiconductors have been reported and the mechanism has not been studied in detail. Crystallographically oriented pore growth has been observed in a variety of III-V semiconductors [4-11] but differences in pore initiation and growth directions as a function of the experimental parameters have not been fully explained and the relationship of sub-surface porosity to pore nucleation at the surface is not well understood. Porous domains, *i.e.* laterally confined regions where pores show evident features of organization around a central structure, have been observed in some instances during the initial stages of porous layer growth. Distinct domains have been observed in GaAs and GaP [4,15]. In GaAs, the domains were reported to be square in plan view; in GaP, however, the domains were reported to be semicircular in cross-section suggesting isotropic pore growth beneath the surface.

We have elsewhere reported [16] the formation of a nanoporous sub-surface region when highly doped ($>10^{18}$ cm^{-3}) n-InP is anodized in aqueous KOH. The nanoporous region was typically 1 – 3 μm in thickness depending on the formation conditions and occurred beneath a thin (typically ~40 nm), dense, near-surface layer. The porosity was approximately 35%. Transmission electron

microscopy (TEM) and atomic force microscopy (AFM) evidence was obtained that the nanoporous layer structure is formed by penetration of surface pits into the InP at particular points and pore propagation originating at these points.

This paper presents results of an investigation of the early stages of the anodic formation of nanoporous structures in n-InP in aqueous KOH, including the observation by TEM of nanoporous domains and evidence of their relationship to surface pits observed by atomic force microscopy (AFM).

Experimental

The working electrode and electrochemical cell have been previously described [16]. Briefly, the working electrode consisted of polished (100)-oriented sulfur-doped n-type indium phosphide (n-InP) grown by the liquid-encapsulated Czochralski (LEC) method and supplied by Sumitomo Electric unless otherwise stated. As-received polished wafers had an essentially featureless surface when viewed at a magnification of 1000X under an optical microscope with Nomarski interference contrast (i.e. a typical surface finish for substrates for epitaxial growth). The nominal density of surface defects of the LEC wafers, as characterized by the etch-pit density (EPD), was in the 10^3 cm^{-2} range or lower. Wafers were cleaved into coupons (typically ~5 mm square) along the natural (110) cleavage planes and an ohmic contact was made by alloying indium to the back of the coupons. The back and the cleaved edges were electrically isolated from the electrolyte by means of a suitable varnish. The electrode area was typically 0.2 cm^2. The carrier concentration was ~3 × 10^{18} cm^{-3}. The electrolyte was 5 mol dm^{-3} KOH and a conventional three-electrode cell configuration was used employing a platinum counter electrode and saturated calomel electrode (SCE) to which all potentials are referenced. All electrochemical experiments were carried out at room temperature and in the absense of light.

A CH Instruments Model 650A Electrochemical Workstation interfaced to a Personal Computer (PC) was employed for cell parameter control and for data acquisition. All linear potential sweep (LPS) experiments were carried out at a scan rate of 2.5 mV s^{-1}. The surfaces of the anodized samples were examined using a Veeco Explorer AFM in non-contact mode with a silicon nitride tip. TEM samples were prepared as previously described [16] using a FEI 200 FIBSIMS workstation and examined using a JEOL 2000FX TEM operating at 200 kV. Spectroscopic ellipsometry was performed using a J. A. Woollam Co., Inc. M-2000U variable angle spectroscopic ellipsometer (VASE) over a wavelength range of 250 – 900 nm.

Results and Discussion

1. Surface Film Growth: TEM and VASE

Fig. 1 shows a linear sweep voltammogram (LSV) of an n-InP electrode in 5 mol dm^{-3} KOH. The current densities observed in the potential range 0 V to 0.35 V are quite low indicating correspondingly low rates of electrochemical reaction. Visual inspection and optical microscopy of the resulting surfaces showed them to be specularly reflecting with very few features apparent.

Fig. 2 shows a cross-sectional TEM image of an InP electrode following an LPS from 0 V to 0.35 V. It is observed that the InP is covered by a thin surface film (A) of thickness 15-20 nm. The thickness of the film is non-uniform, in agreement with AFM observations of surface undulations that will be discussed in Section 2. Thus, an LPS from 0 V to 0.35 V results in the formation of a thin surface film, which appears to be relatively compact. The (011) projection electron diffration pattern is shown in the inset to Fig. 2. The diffraction ring corresponds to In_2O_3 in the surface film.

VASE was employed to characterize the growth of surface films below 0.35 V. LPS experiments from 0 V to upper potentials in the range 0.1 V – 0.35 V were carried out on a series of InP electrodes. After anodization, electrodes were rinsed and dried and the ellipsometric data

was acquired *ex situ* in the wavelength range 250 – 900 nm at incident angles of 65º, 70º and 75º. A typical plot of the measured ellipsometric parameters, Ψ and Δ, as a function of wavelength is shown in Fig. 3 for an upper potential of 0.35 V. The solid lines represent simulated data modeled assuming a compact In_2O_3 film with a thickness value optimized to provide best fit to the experimental data. It can be observed that a good fit has been achieved over the whole wavelength range. The thickness value obtained is 15 nm.

Values of film thickness were similarly measured for the other electrodes in the series. The resulting thickness values are plotted against upper potential in Fig. 4. It can be seen that the film thickness increases with potential from ~4.5 nm at 0.1 V to ~15 nm at 0.35 V. Furthermore, it was found that no reliable data could be acquired when the upper potential was greater than ~0.38 V suggesting possible changes in the surface morphology occurring at higher potentials.

2. AFM Studies of Surface Morphology and Pitting

AFM was employed also to characterize the surface of the electrodes after anodization. A typical AFM image of the surface of an electrode following an LPS from 0 V to 0.35 V is shown in Fig. 5a. An image of a typical as-received InP wafer is shown for comparison in Fig. 5b. It is clear that anodization to this potential has caused relatively little surface modification. The average root-mean-square (rms) roughness was estimated for both samples from the AFM data and values of 2.4 nm and 0.88 nm were obtained for the anodized and as-received samples respectively. Thus, anodization of electrodes to upper potentials of ~0.35 V or less results in some surface modification and a modest increase in roughness. However, there is no evidence of pit formation.

Electrodes subjected to LPSs with upper potentials in the range 0.4 V to 0.53 V were also studied by AFM. Fig. 6a shows an AFM image of the surface of an electrode following an LPS from 0 V to 0.425 V. The image clearly shows an etch pit that has formed on the surface. Similar

pits were observed in AFM images obtained in other LPS experiments with upper potentials in the range 0.4 V to 0.53 V. For example, an image obtained for 0.48 V (*i.e.* at the current peak) is shown in Fig. 6b. Line scans through the AFM images in Figs. 6a and 6b are shown in Figs. 6c and 6d respectively. Although the AFM cannot accurately profile deep pits, we can obtain some estimate of the diameter of the pits from these traces. Thus, taking the value of the full width at half maximum from these traces we obtain a value of ~50 nm for the pit diameter in each case. This approximate measurement is in agreement with observations in cross-sectional TEM images [16], where channels through the near-surface layer have similar width.

Similar pits were observed in AFM images of electrodes that had been anodized at constant potential: a typical image after anodization at 0.5 V for 25 s is shown in Fig. 7. Again, a pit similar to those shown in Fig. 6 can be observed. Images at other anodization times showed similar pits.

Estimates were made of the areal density of pits on electrode surfaces after anodization under potentiodynamic conditions. A series of experiments was carried out in which electrodes were subjected to LPSs from 0 V to upper potentials in the range 0.40 V to 0.53 V and 10 μm × 10 μm AFM images were obtained of the resulting surfaces. A typical such image is shown in Fig. 8 for 0.48 V (corresponding to the current peak). At this lower magnification, multiple pits are visible on the surface. By counting the pits (~23 for this image) the areal density of pits on the surface (2.3×10^7 cm^{-2} in this case) can be estimated. Estimates of pit density were similarly obtained from AFM images of electrodes anodized to various upper potentials and the average value of pit density was obtained in each case. Results are plotted in Fig. 9: the corresponding portion of the LSV is shown for comparison. It is clear that the density of pits on the surface increases progressively with increasing potential. The rate of increase of pit density is greatest in the vicinity of 0.45 V, which corresponds to half the peak current. Above ~0.48 V (*i.e.* the potential of peak current) the pit density begins to plateau at a value of ~2.5×10^7 cm^{-2} and further increase in pit

density is small. Thus, the rising portion of the current peak corresponds to a progressive increase in density of surface pits; when the current maximum is reached, no further significant increase in pit density is observed.

A similar study was conducted on electrodes following anodization at constant potential. A typical image of a surface after anodization at 0.5 V for 25 s is shown in Fig. 10. Images of surfaces after other anodization times were similarly obtained. Resulting values of pit density and corresponding current density obtained at 0.5 V are plotted against anodization time in Fig. 11. The pit density increases with time and approaches a plateau value of ~9×10^6 cm^{-2} after 20-30 s showing that surface pitting occurs progressively at constant potential in a similar manner to that observed under LPS conditions. Thus, channels in the near-surface layer that are believed to be the pathways for electrolyte access to the nanoporous region form progressively in time and, as shown below, this has an important role in the growth of the sub-surface nanoporous layer.

3. TEM Observations of Pore Growth

In order to investigate the mechanism by which porosity develops in n-InP under anodic conditions in 5 mol dm^{-3} KOH, experiments were carried out in which the potential was swept from 0 V to 0.44 V and the electrode was then cross-sectioned and examined. A TEM micrograph of such a cross-section (Fig. 12) shows that individual nanoporous domains have formed that have a triangular cross-section with the base of the triangle parallel to the InP surface. The nanoporous domain is separated from the surface by a thin (~40 nm) dense near-surface layer as was observed for the more fully developed nanoporous layer [16].

The cross-section in Fig. 12 is in a {110} cleavage plane. Other TEM micrographs show that the nanoporous domains have 'dove-tail' (trapezium-shaped) cross-sections in the other (orthogonal) {110} cleavage plane. Fig. 13 shows a plan-view TEM micrograph of a slice through

the InP in the {100} plane, parallel to the surface and ~100 nm below it. Nanoporous domains with approximately square outlines are clearly visible. We suggest that each domain originates from a single channel through the near-surface layer. We will show elsewhere [17] that <111> directional growth of pores from such an origin leads to domain shapes consistent with the observed cross-sections.

4. Progressive Pit Nucleation and Domain Merging

As discussed earlier, AFM examination shows a distribution of pits on the electrode surface after anodization, the density of which increases progressively with time (Figs. 9 and 11) and it is suggested that each of these pits acts as a source for a nanoporous domain. Thus, the initiation of new nanoporous domains beneath the surface must also be progressive in time (rather than instantaneous). Evidence for this can be seen in Fig. 13 and in Fig. 14, which shows a plan view TEM image of an adjacent area of the same electrode as in Fig. 13. It can be seen that the nanoporous domains are at various stages of development. In particular, in Fig. 14 it can be seen that merging of some domains has occurred (bottom left) while other domains are at very early stages of growth.

It is postulated that new pits are formed only in areas where bulk (non-porous) InP still remains immediately beneath the surface, so that there is a high electric field at the electrode-electrolyte interface. Thus the plateau in pit density occurs when the underlying nanoporous domains have grown large enough so that their bases begin to touch and cover the area. Thus, TEM provides further evidence that development of the nanoporous layer occurs by the merging of individual nanoporous domains that have a one-to-one correspondence with progressively formed surface pits.

The progressive formation of nanoporous domains is shown conclusively in Fig. 15a, which is a plan view TEM micrograph of an electrode following an LPS to 0.48 V. Numerous domains are visible and some are considerably more developed than others. Furthermore, in some areas, considerable domain merging has occurred. A cross-sectional TEM of an electrode anodized under the same conditions is shown in Fig. 15b. This image was acquired from a region where domains were seen to merge. The image suggests that a number of nanoporous domains are overlapping. Incidentally, direct evidence for the presence of a channel in the near-surface layer at the center of the domain base is evident at 'A' in Fig. 15b. Thus, merging of domains continues to occur at potentials more anodic than the peak potential, where the current is observed to decrease.

The proposed model is consistent with the current-potential behavior observed in LPS experiments and the current-time behavior at constant potential. Analysis of the cyclic voltammograms of InP electrodes in 5 mol dm^{-3} KOH indicates [18] that, once a critical potential for pore formation is reached, the anodic current is predominantly dependent on time rather than potential. With increasing time, as the density of surface pits increases and each pit gives rise to a growing nanoporous domain, the current correspondingly increases. Eventually the density of surface pits and domains reaches a constant value.

Fig. 16a shows values of current density from Fig. 9 plotted against the corresponding values of pit density. It can be seen that the current density increases approximately linearly with pit density up to a value of ~2.5×10^7 cm^{-2} and thereafter decreases sharply. The least squares best fit lines for the first 8 points and the last 4 points respectively (in order of increasing pit density) are shown and it can be seen that these give a reasonable representation of the trend. From the ratio of current density to pit density, the average current per pit (channel) can be estimated. This was done for both the experimental points and the trend lines in Fig. 16a and the results are shown in Fig. 16b. Although there is considerable scatter, it can be seen that the average current per pit increases from

~0.3 nA at 0.4 V to a maximum of ~ 0.8 nA at ~0.48 V and thereafter decreases.

Similar plots for the constant potential data from Fig. 11 are shown in Fig 17. Again, the current density increases approximately linearly with pit density up to a critical value and thereafter decreases sharply (Fig 17a). As seen earlier in Fig. 11, the critical (plateau) value (9×10^6 cm^{-2}) in this case is somewhat lower, and the maximum current density value (~40 mA cm^{-2}) is somewhat higher, than in the case of the LPS results in Fig 16a. Fig 17b shows that the average current per pit increases somewhat from ~4 nA at 5 s to a maximum of ~5 nA at ~25 s and thereafter decreases. These values are higher than those for the LSV in Fig. 17b. The differences in values between Figs 16 and 17 are not surprising since the current density depends on scan rate in the case of the LSV results and on the value of potential in the case of the constant potential results.

As a domain grows, the number of growing pore tips increases and consequently the corresponding current increases. Each point in Fig 16b (and in Fig. 17b) represents an average value of current for a distribution of pits, each of which corresponds to a channel that is a current feed point for a growing nanoporous domain. Thus each value of current shown is an average for a distribution of pits with a corresponding distribution of domain sizes. Newly formed pits are expected to have smaller underlying domains and correspondingly smaller currents than older pits. Thus, the increase in average current per pit in Fig. 16b (and in Fig. 17b) is consistent with an increasing fraction of older, larger domains in the distribution with increasing time. Eventually, adjacent domains merge as they grow larger. Since this must limit the growth of a domain to regions not already ‘occupied’, the current corresponding to these domains decreases and so the current per pit decreases. This is seen at potentials greater than 0.48 V in Fig. 16b and at times greater than 25 s in Fig. 17b. Ultimately, the domains merge into a continuous nanoporous layer.

It is clear from Fig. 16 that the current in a typical channel through the near-surface layer is on

the order of 1 nA. This corresponds to a current density of ~80 A cm^{-2} for a channel of width of ~40 nm. However, for such a channel of length 40 nm the electrolyte resistance is < 1 MΩ (based on a resistivity [19] of < 3 Ω cm for 5 mol dm^{-3} KOH) and so the potential difference for a 1 nA current is less than 1 mV. The pit currents (and corresponding current densities) for the case of a constant potential of 0.5 V (Fig. 17) are larger by about an order of magnitude than in the corresponding LPS case (Fig. 16) but, even so, the estimated potential difference across the channel is less than 10 mV. Thus, the estimated high values of current density in channels are reasonable. Beneath the near-surface layer, the current will divide between the multiple pores into which the channel branches so that the current density in each is considerably lower.

Conclusions

The early stages of nanoporous layer formation under anodic conditions have been investigated for n-type InP with a carrier concentration of ~3×10^{18} cm^{-3} in 5 mol dm^{-3} KOH and a mechanism for the process is proposed.

The current densities in LSVs in the potential range 0 V to 0.35 V were observed to be quite low and both visual inspection and optical microscopy of the resulting surfaces showed them to be specularly reflecting with very few features apparent. TEM cross-sections of electrodes anodized to 0.35 V show a somewhat non-uniform oxide film, 15 – 20 nm in thickness, on the surface. VASE shows an increase in film thickness with potential from ~4.5 nm at 0.1 V to ~15 nm at 0.35 V. AFM of electrode surfaces after LPSs to upper potentials less than ~0.35 V show some surface modification and a modest increase in roughness but no evidence of pit formation.

For upper potentials in the range 0.4 V to 0.53 V, AFM images clearly show etch pit formation on the surface. Approximate estimates of pit size are in agreement with estimates of the width of channels through the near-surface layer observed in TEM cross-sections. The density of pits was

shown to increase progressively with potential in the range corresponding to the rising anodic peak in the voltammogram. The rate of increase is greatest in the vicinity of 0.45 V which corresponds to half the peak current. Above ~0.48 V (*i.e.* the potential of peak current) the pit density begins to plateau. Results obtained by AFM for a constant potential of 0.5 V show that surface pitting occurs progressively with time in a similar manner to that observed under LPS conditions.

TEM clearly shows individual nanoporous domains in electrode cross-sections. The cross-sections also show that the domains are separated from the surface by a dense InP layer, ~40 nm in thickness, similar to that observed at the later stages of nanoporous layer formation. It is concluded that each domain develops as a result of directionally preferential pore propagation from an individual surface pit which forms a channel through this near-surface layer.

Since the AFM measurements show that the density of surface pits increases progressively with time and each of these pits acts as a source for an individual nanoporous domain, the development of these domains beneath the surface must also be progressive in nature. Evidence for this is seen in plan view TEM images that clearly show individual domains at various stages of development. As they grow larger, domains meet and the merging of multiple domains eventually leads to a continuous nanoporous sub-surface region.

The proposed model is consistent with the current-time behavior observed during LPS and constant potential experiments. Initially the current increases as surface pits are nucleated and each pit gives rise to a growing nanoporous domain. Eventually, no further new domains are formed and existing domains meet and merge resulting in a decrease in current.

List of Acronyms and Abbreviations.

AFM: atomic force microscopy

LPS: linear potential sweep

LSV: linear sweep voltammogram

n-InP: n-type indium phosphide

SCE: saturated calomel electrode

TEM: transmission electron microscopy

VASE: variable angle spectroscopic ellipsometry

Acknowledgements.

We gratefully acknowledge Enterprise Ireland, the Programme for Research in Third Level Institutions (PRTLI) of the Irish Higher Education Authority (HEA) and the Materials and Surface Science Institute (MSSI) for their support. We are also grateful to Vistakon Ireland Ltd. for the provision of laboratory facilities and to Dr S. M. Parle for technical assistance.

References

[1] B. H. Erne, D. Vanmaekelbergh and J. J. Kelly, *J. Electrochem. Soc.*, **143**, 305 (1996)

[2] J. Carstensen, M. Christophersen and H. Föll, *Mater. Sci. Eng. B*, **69-70**, 23 (2000)

[3] S. Langa, J. Carstensen, I. M. Tiginyanu, M. Christophersen and H. Föll, *Electrochem. Solid-State Lett.*, **5**, C14 (2002)

[4] S. Langa, J. Carstensen, M. Christophersen, H. Föll, and I. M. Tiginyanu, *Appl. Phys. Lett.*, **78**, 1074 (2001)

[5] G. Oskam, A. Natarajan, P. C. Searson and F. M. Ross, *Appl. Surf. Sci.*, **119**, 160 (1997)

[6] M. M. Faktor, D. G. Fiddyment and M. R. Taylor, *J. Electrochem. Soc.*, **122**, 1566 (1975)

[7] F. M. Ross, G. Oskam, P. C. Searson, J. M. Macaulay and J. A. Liddle, *Philos. Mag. A*, **75**, 2 (1997)

[8] C. O'Dwyer, D. N. Buckley, V. J. Cunnane, D. Sutton, M. Serantoni and S. B. Newcomb, in *Proceedings of the State-of-the-Art Program on Compound Semiconductors XXXVII*, PV **2002-14**, p. 259, The Electrochemical Society, Proceedings Series, Pennington, NJ (2002)

[9] S. Langa, J. Carstensen, I. M. Tiginyanu, M. Christophersen and H. Föll, *Electrochem. Solid-State Lett.*, **4**, G50 (2001)

[10] S. Langa, I. M. Tiginyanu, J. Carstensen, M. Christophersen and H. Föll, *Electrochem. Solid-State Lett.*, **3**, 514 (2000)

[11] E. Harvey, C. O'Dwyer, T. Melly, D. N. Buckley, V. J. Cunnane, D. Sutton, S. B. Newcomb and S. N. G. Chu, in *Proceedings of the State-of-the-Art Program on Compound Semiconductors XXXV*, PV **2001-2**, p. 87, The Electrochemical Society, Proceedings Series, Pennington, NJ (2001)

[12] V. Lehmann, *J. Electrochem Soc.*, **140**, 2836 (1993)

[13] P. Schmuki, L. E. Erikson, D. J. Lockwood, B. F. Mason, J. W. Fraser, G. Champion, and H. J. Labbe, *J. Electrochem. Soc.*, **146**, 735 (1999)

[14] I. M. Tiginyanu, C. Schwab, J.-J. Grob, B. Prevot, H. L. Hartnagel, A. Vogt, G. Irmer, and J. Monecke, *Appl. Phys. Lett.*, **71**, 3829 (1997)

[15] R. W. Tjerkstra, J. Gomez-Rivas, D. Vanmaekelbergh, and J. J. Kelly, *Electrochem. Solid-State Lett.*, **5**, G32 (2002)

[16] C. O'Dwyer, D. N. Buckley, D. Sutton, and S. B. Newcomb, *J. Electrochem. Soc.*, accepted for publication, MS. No. JES-06-0674R

[17] R. Lynch, C. O'Dwyer, D. N. Buckley, D. Sutton and S. B. Newcomb, *Electrochem. Solid-State Lett.* (to be submitted)

[18] C. O'Dwyer, D. N. Buckley, M. Serantoni, D. Sutton, and S. B. Newcomb, in *Proceedings of the State-of-the-Art Program on Compound Semiconductors XXXIX*, PV **2003-11**, p. 136, The Electrochemical Society, Proceedings Series, Pennington, NJ (2003)

[19] Landolt-Bornstein, *Zahlenwerte und Funktionen*, 6th Ed., Vol. II, Part 7 "Elektrische Eigenschaften II", pp. 36, 54 and 87 (Springer-Verlag, Berlin, 1960); L. F. Darken and H. F. Meier, *J. Am. Chem. Soc*., **64**, 621 (1942); G. Grube and A. Vogt, *Z. Elektrochem*. **44**, 353 (1938)

Figure captions

Fig. 1. LSV at 2.5 mV s^{-1} of an n-InP electrode in 5 mol dm^{-3} KOH.

Fig. 2. Cross-sectional bright-field TEM micrograph of an InP electrode after LPS anodization from 0 V to 0.35 V (SCE) in 5 mol dm^{-3} KOH at 2.5 mV s^{-1}. The inset shows the corresponding electron diffraction pattern.

Fig. 3. (Color online) Variation of the ellipsometric parameters Ψ and Δ as a function of wavelength for a surface film formed on InP after an LPS from 0 V to 0.35 V in 5 mol dm^{-3} KOH at 2.5 mV s^{-1}. Data is shown for angles of 65º, 70º and 75º. The solid lines represent the fitted data assuming an In_2O_3 film.

Fig. 4. Surface film thickness plotted against potential for n-InP electrodes after an LPS at 2.5 mV s^{-1} in 5 mol dm^{-3} to upper potentials in the range 0 V to 0.35 V (SCE). The film thickness was measured using spectroscopic ellipsometry assuming a compact In_2O_3 layer.

Fig. 5. AFM images of the surface of an InP electrode (a) after an LPS from 0 V to 0.35 V (SCE) in 5 mol dm^{-3} KOH at 2.5 mV s^{-1} and (b) an as-received InP wafer.

Fig. 6. (Color online) AFM images of the surface of an InP electrode after an LPS at 2.5 mV s^{-1} in 5 mol dm^{-3} KOH from 0 V to (a) 0.425 V, (b) 0.48 V (SCE); (c) Line scan of the pore shown in (a); and (d) line scan of the pore shown in (b).

Fig. 7. (Color online) AFM image of the surface of an InP electrode after anodization at a constant potential of 0.5 V (SCE) for 25 s in 5 mol dm^{-3} KOH.

Fig. 8. (Color online) AFM image of the surface of an InP electrode after an LPS from 0 V to 0.48 V (SCE) at 2.5 mV s^{-1} in 5 mol dm^{-3} KOH.

Fig. 9. Areal density of surface pits (●) on InP electrodes, following an LPS from 0 V (SCE), plotted against the upper potential. The line shows the corresponding LSV. The scan rate was 2.5 mV s^{-1} and the electrolyte was 5 mol dm^{-3} KOH. Pit densities were determined from 10 μm × 10 μm AFM images.

Fig. 10. (Color online) AFM image of the surface of an InP electrode after anodization at a constant potential of 0.5 V (SCE) for 25 s in 5 mol dm^{-3} KOH.

Fig. 11. Areal density of surface pits (●) on InP electrodes plotted against anodization time at 0.5 V (SCE). The line shows the corresponding current-time curve. The electrolyte was 5 mol dm^{-3} KOH. Pit densities were determined from 10 μm × 10 μm AFM images.

Fig. 12. Cross-sectional bright-field TEM micrograph of an InP electrode after an LPS from 0 to 0.44 V (SCE) in 5 mol dm^{-3} KOH at 2.5 mV s^{-1}. The plane of the micrograph is {110}.

Fig. 13. Plan-view bright-field TEM micrograph of a section through an InP electrode ~100 nm below the surface. Anodization conditions were the same as in Fig. 12. The plane of the micrograph is {100}. Adjacent nanoporous domains are visible.

Fig. 14. Plan-view bright-field TEM micrograph of an adjacent section of the InP electrode in Fig. 13. The plane of the micrograph is {100}. Adjacent and merging nanoporous domains are visible.

Fig. 15. Bright-field TEM micrographs of an InP electrode after an LPS from 0 V to 0.48 V (SCE) at 2.5 mV s^{-1} in 5 mol dm^{-3} KOH. (a) Plan-view section ~100 nm below the surface. The progressive development of the nanoporous domains is apparent. (b) {110} cross-section showing merged nanoporous domains. An etch pit on the surface is observed in cross-section at 'A'.

Fig. 16. (a) Current density during an LPS plotted against the corresponding surface pit density in Fig 9. (b) The corresponding current per pit plotted against potential; the points and the line were estimated from, respectively, the experimental values and the best fit lines in (a). The initial potential was 0 V (SCE), the scan rate was 2.5 mV s^{-1} and the electrolyte was 5 mol dm^{-3} KOH.

Fig 17. (a) Current density at a constant potential of 0.5 V (SCE) plotted against the corresponding surface pit density in Fig 11. (b) The corresponding current per pit plotted against time; the points and the line were estimated from, respectively, the experimental values and the best fit lines in (a). The electrolyte was 5 mol dm^{-3} KOH.

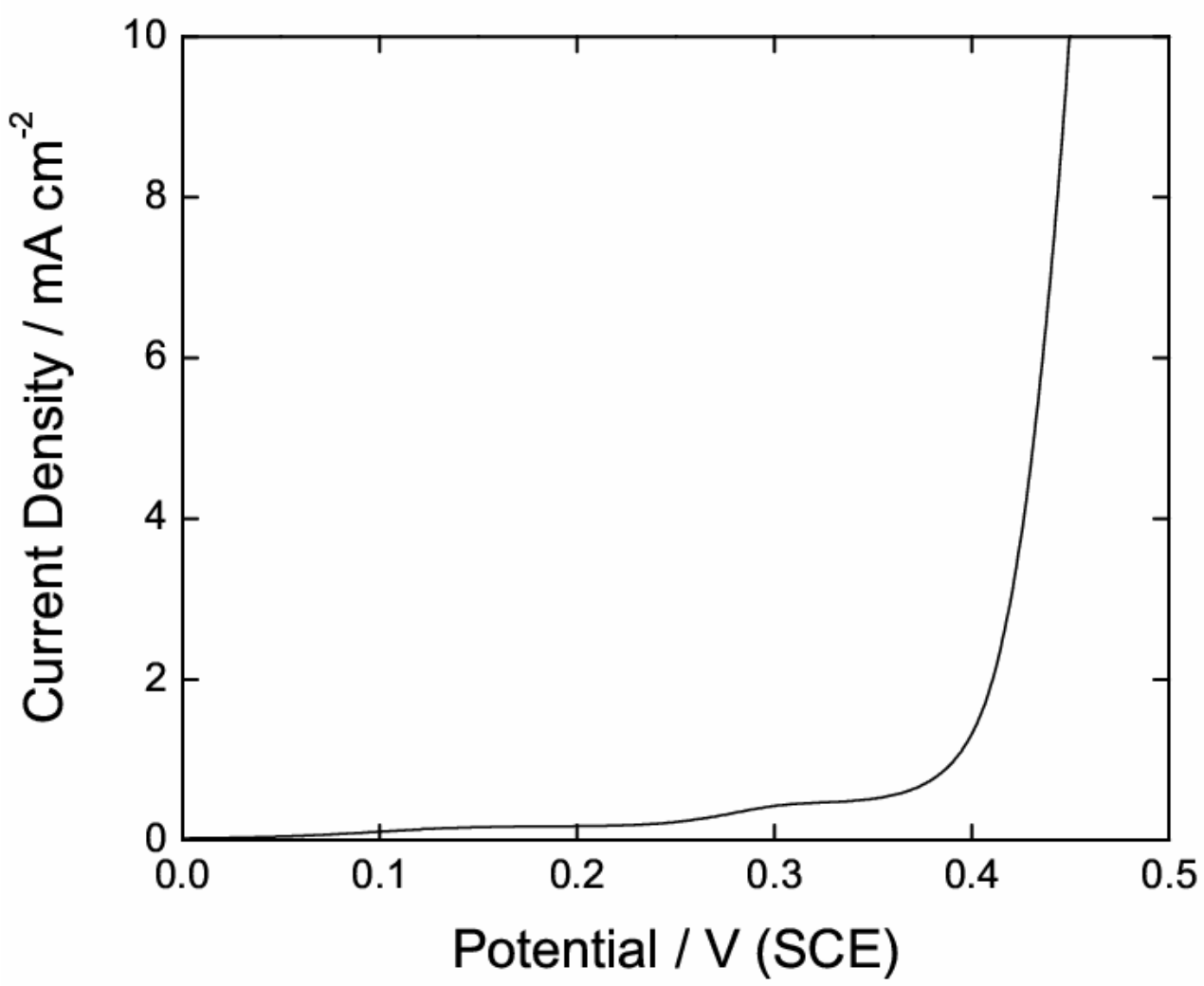
Current Density / mA cm-2
10
8
6
4
2
0
0.0
0.1
0.2
0.3
0.4
0.5
Potential / V (SCE)

Fig. 1

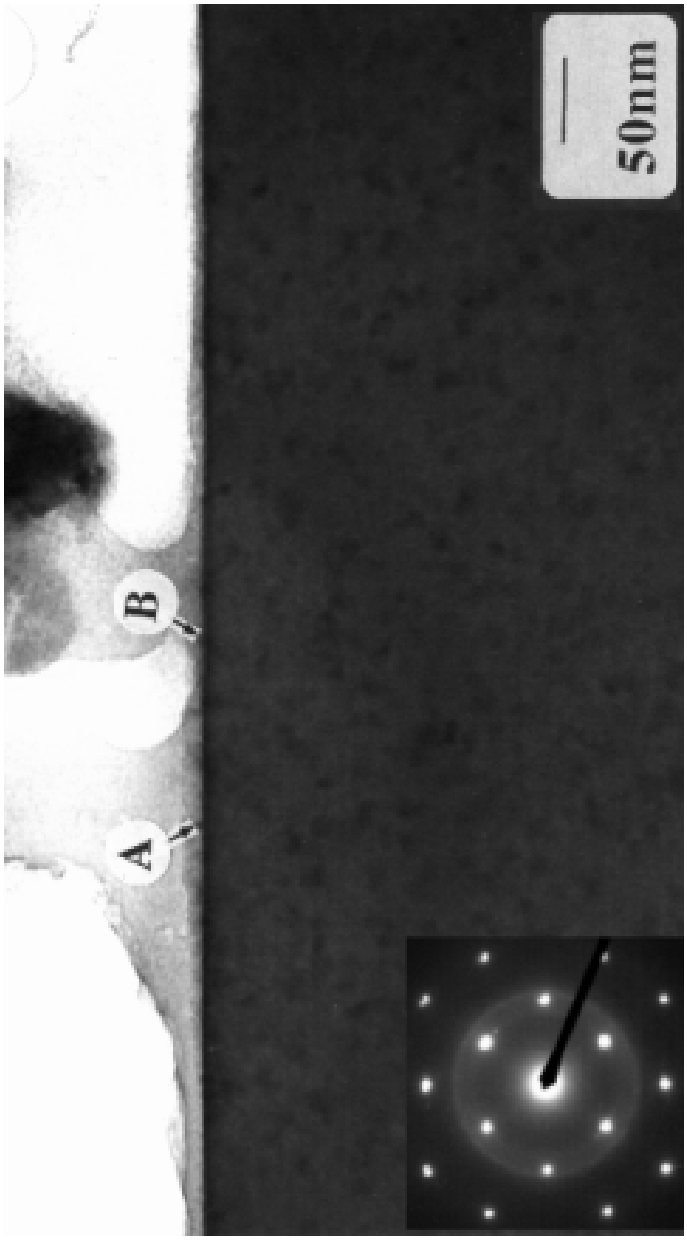

Fig. 2

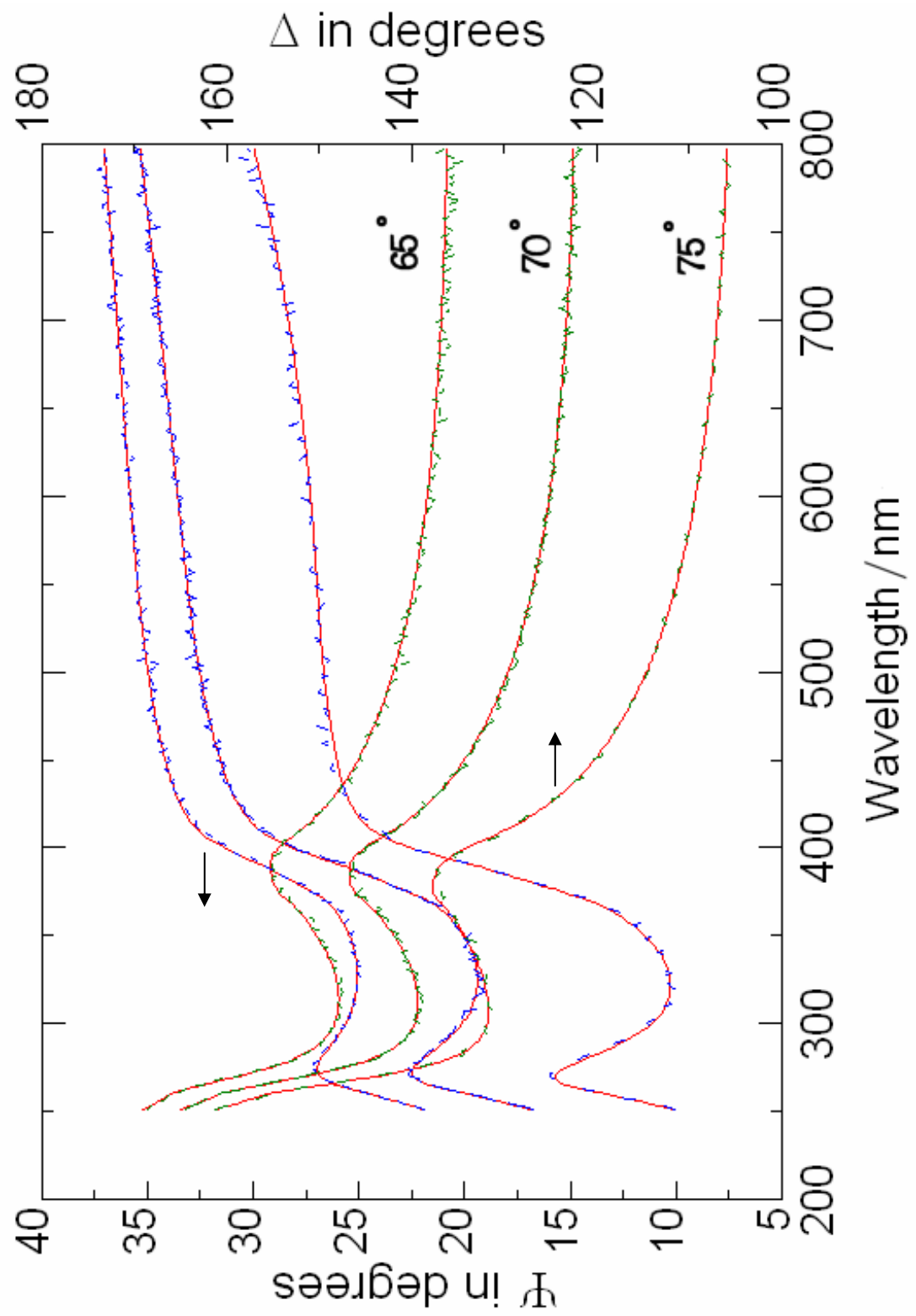
Δ in degrees
180
160
140
120
100
65°
70°
75°
Ψ in degrees
40
35
30
25
20
15
10
5
200
300
400
500
600
700
800
Wavelength / nm

Fig. 3

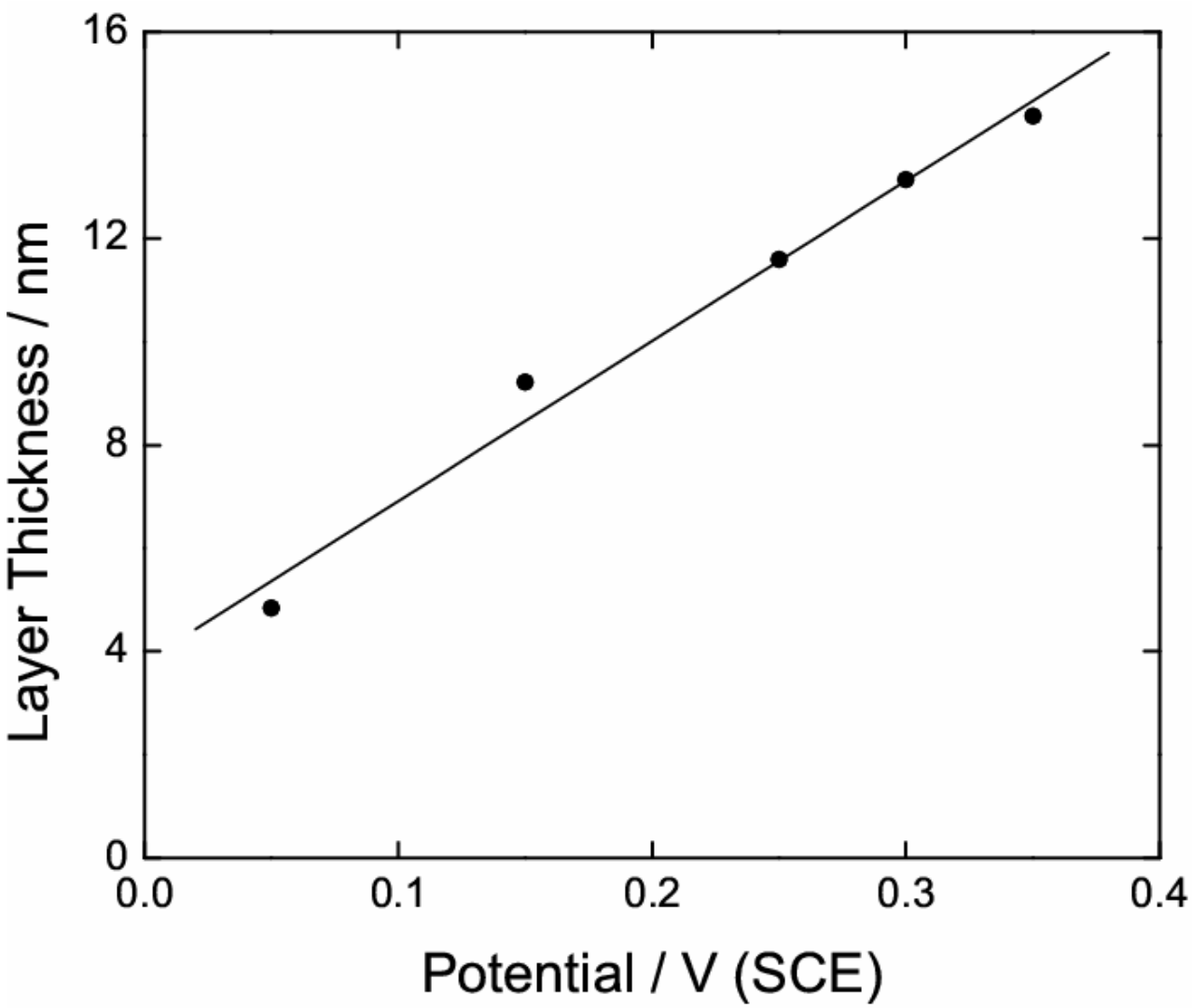

Fig. 4

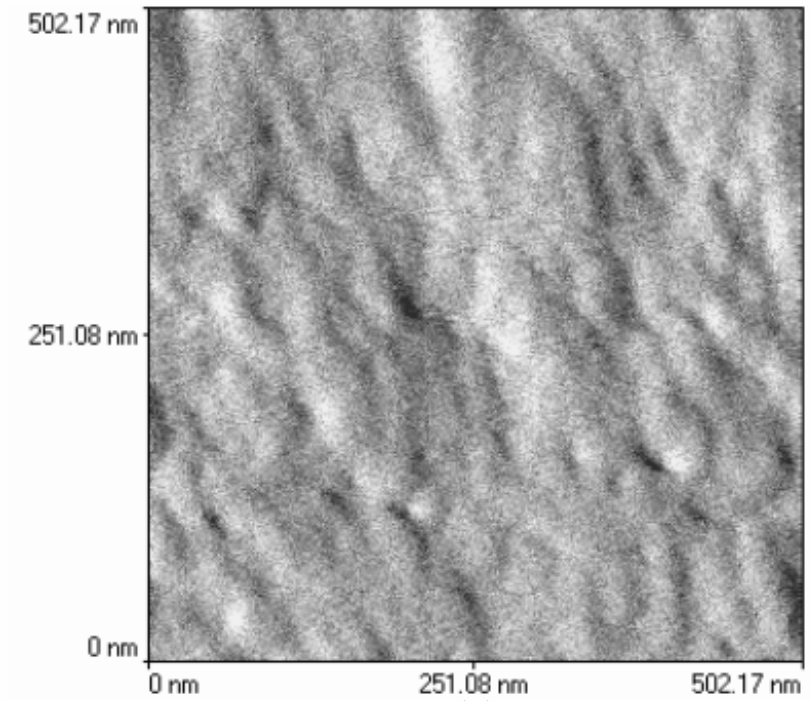
502.17 nm
251.08 nm
0 nm
0 nm
251.08 nm
502.17 nm

(a)

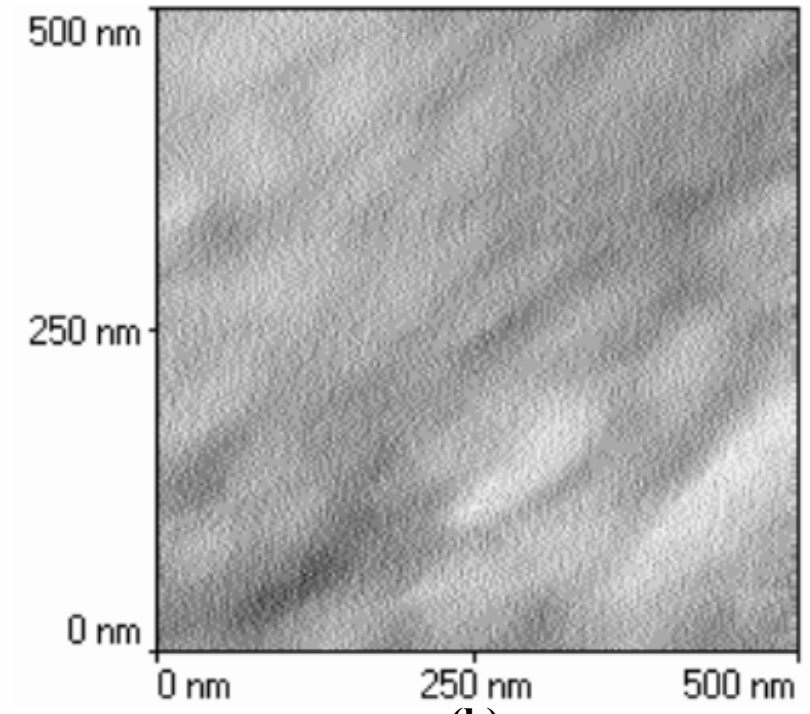
500 nm
250 nm
0 nm
0 nm
250 nm
500 nm

(b)

Fig. 5

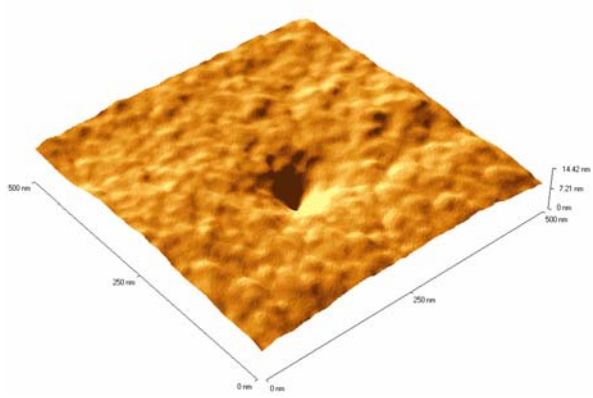
14.42 nm
7.21 nm
0 nm
500 nm
500 nm
250 nm
250 nm
0 nm
0 nm

(a)

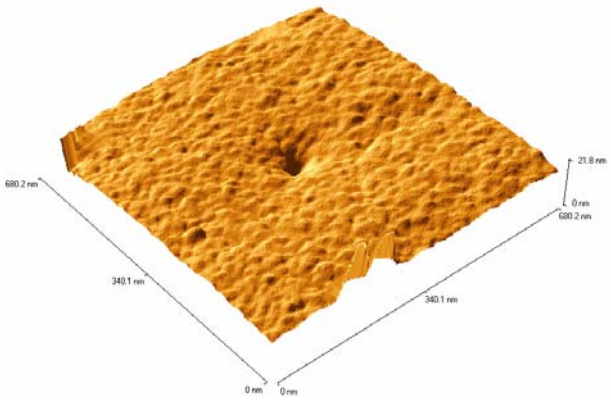
21.8 nm
0 nm
680.2 nm
680.2 nm
340.1 nm
340.1 nm
0 nm
0 nm

(b)

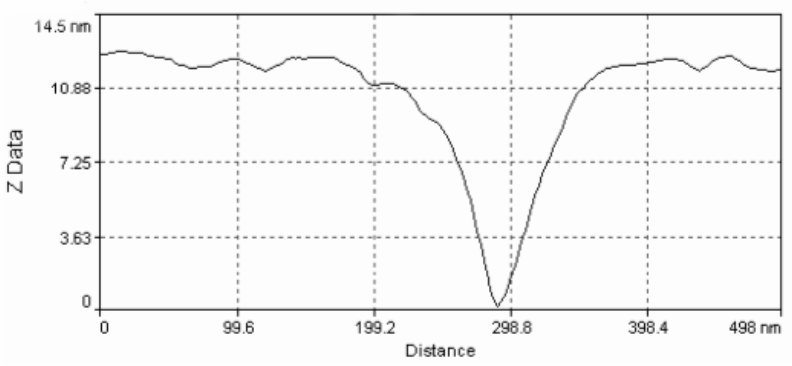
14.5 nm
10.88
7.25
3.63
0
Z Data
0
99.6
199.2
298.8
398.4
498 nm
Distance

(c)

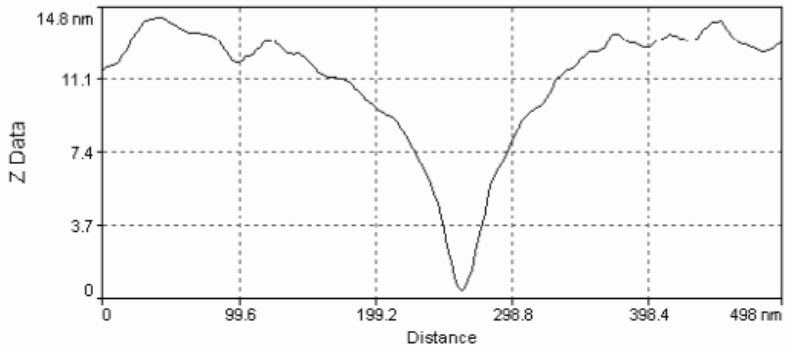
14.8 nm
11.1
7.4
3.7
0
Z Data
0
99.6
199.2
298.8
398.4
498 nm
Distance

(d)

Fig. 6

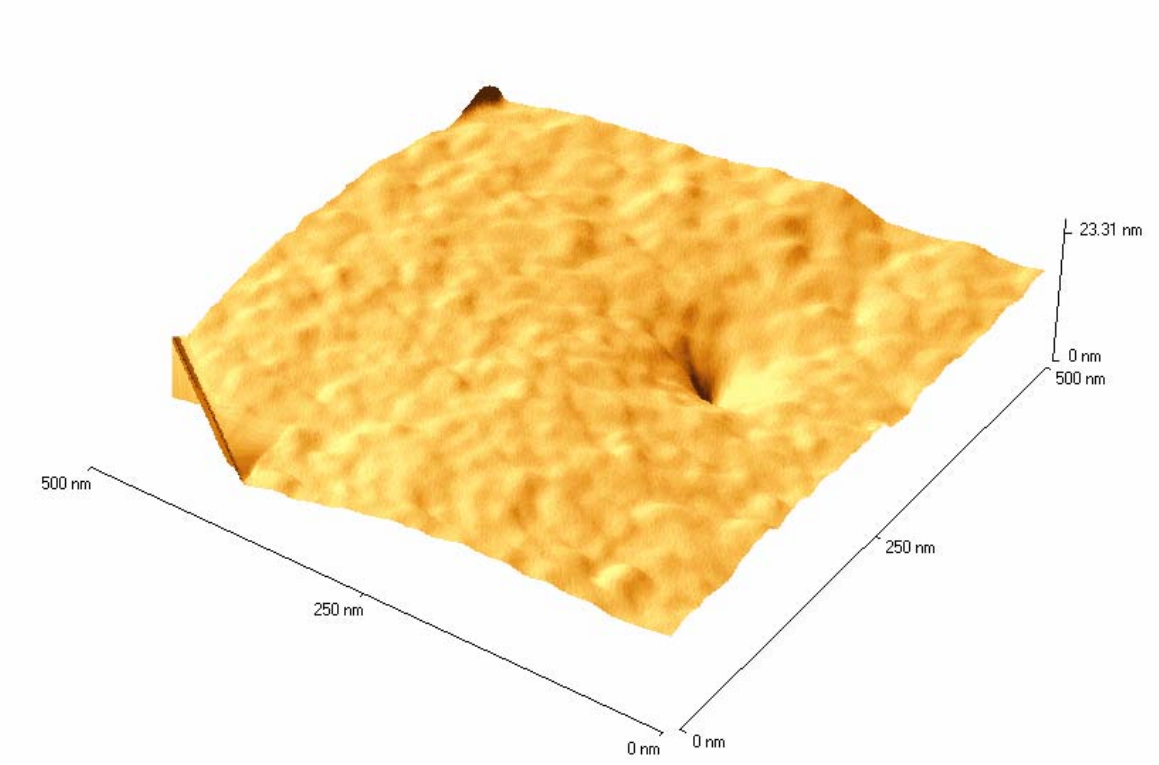

Fig. 7

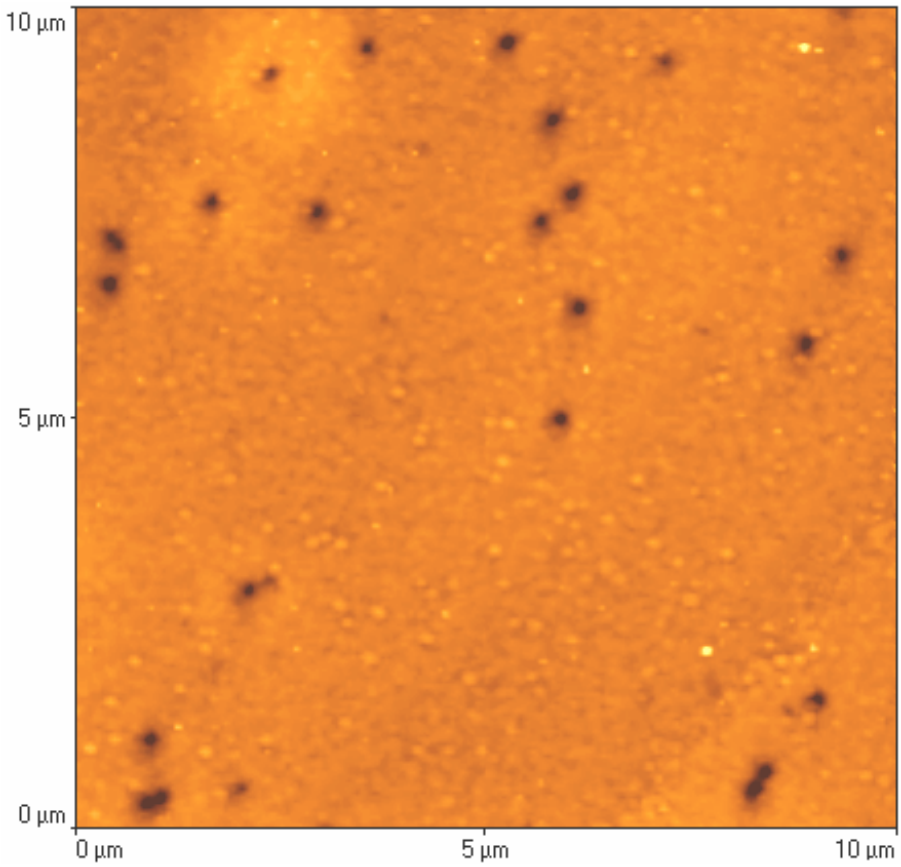

Fig. 8

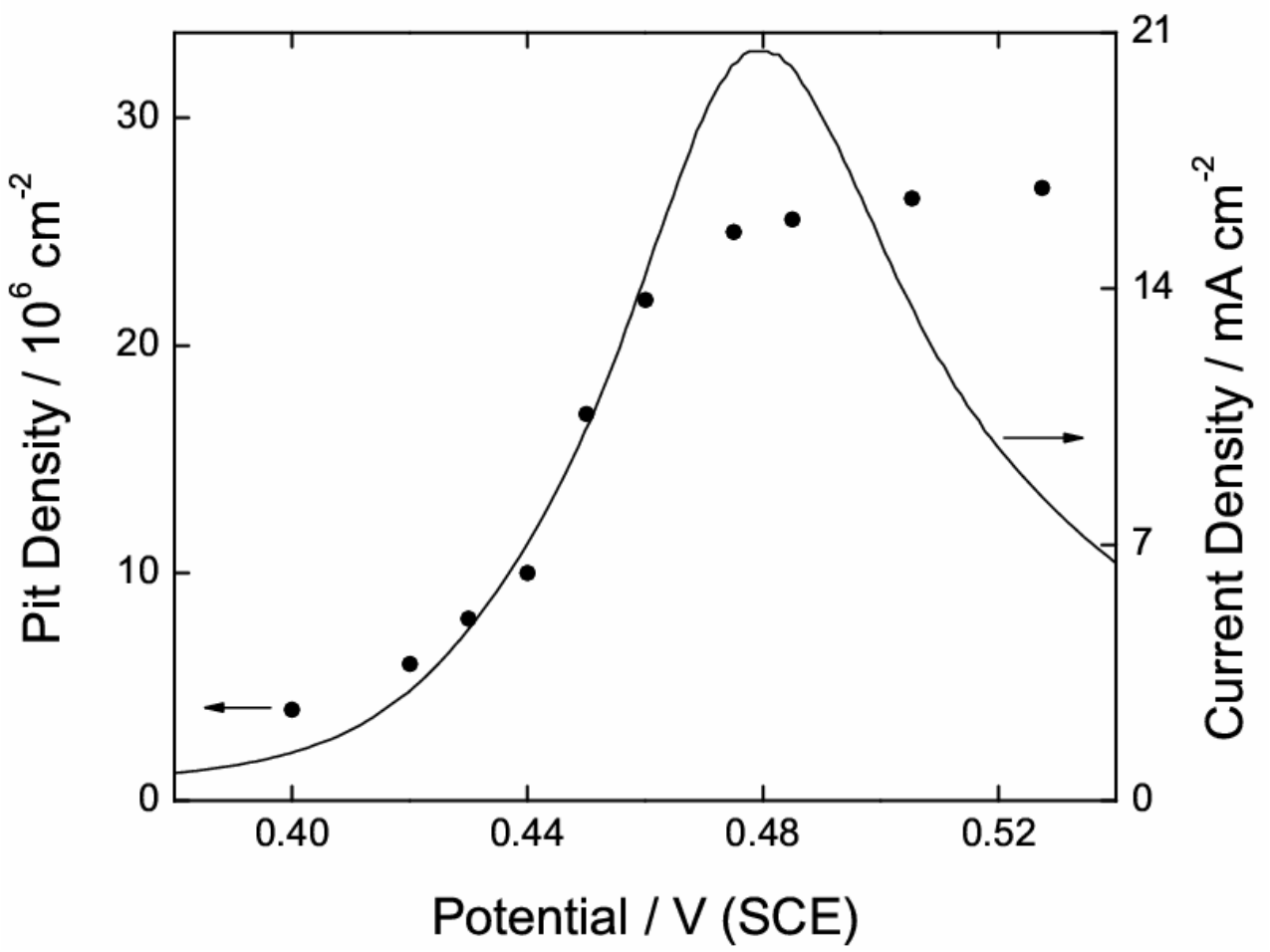
Pit Density / 10^6 cm^-2
Current Density / mA cm^-2
Potential / V (SCE)
0
10
20
30
0
7
14
21
0.40
0.44
0.48
0.52

Fig. 9

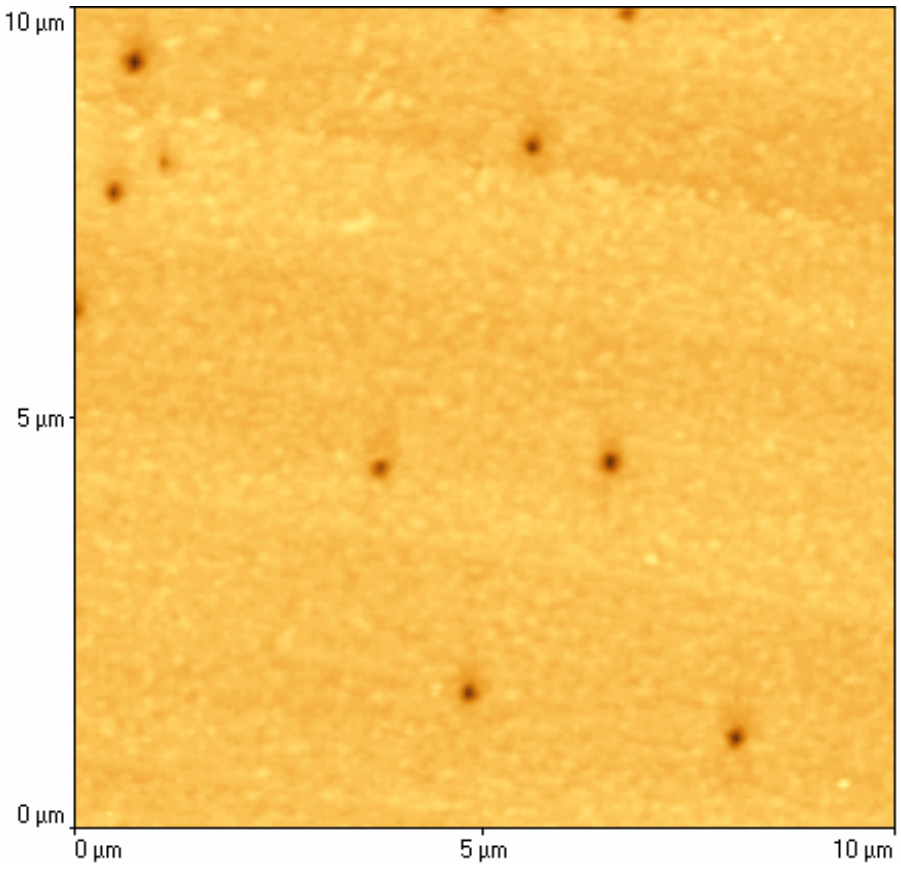

Fig. 10

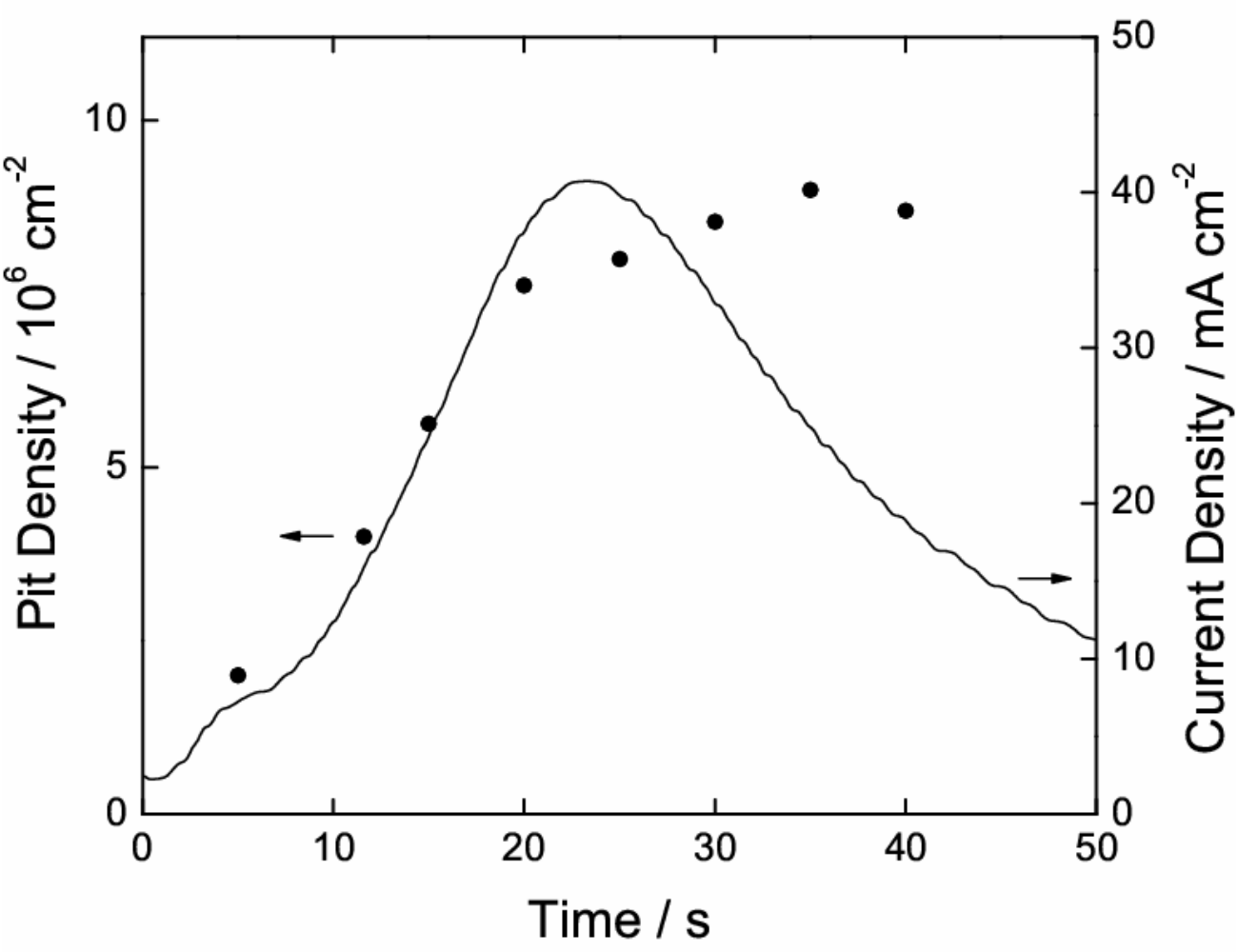
Pit Density / 10^6 cm^-2
Current Density / mA cm^-2
Time / s
0
5
10
0
10
20
30
40
50
0
10
20
30
40
50

Fig. 11

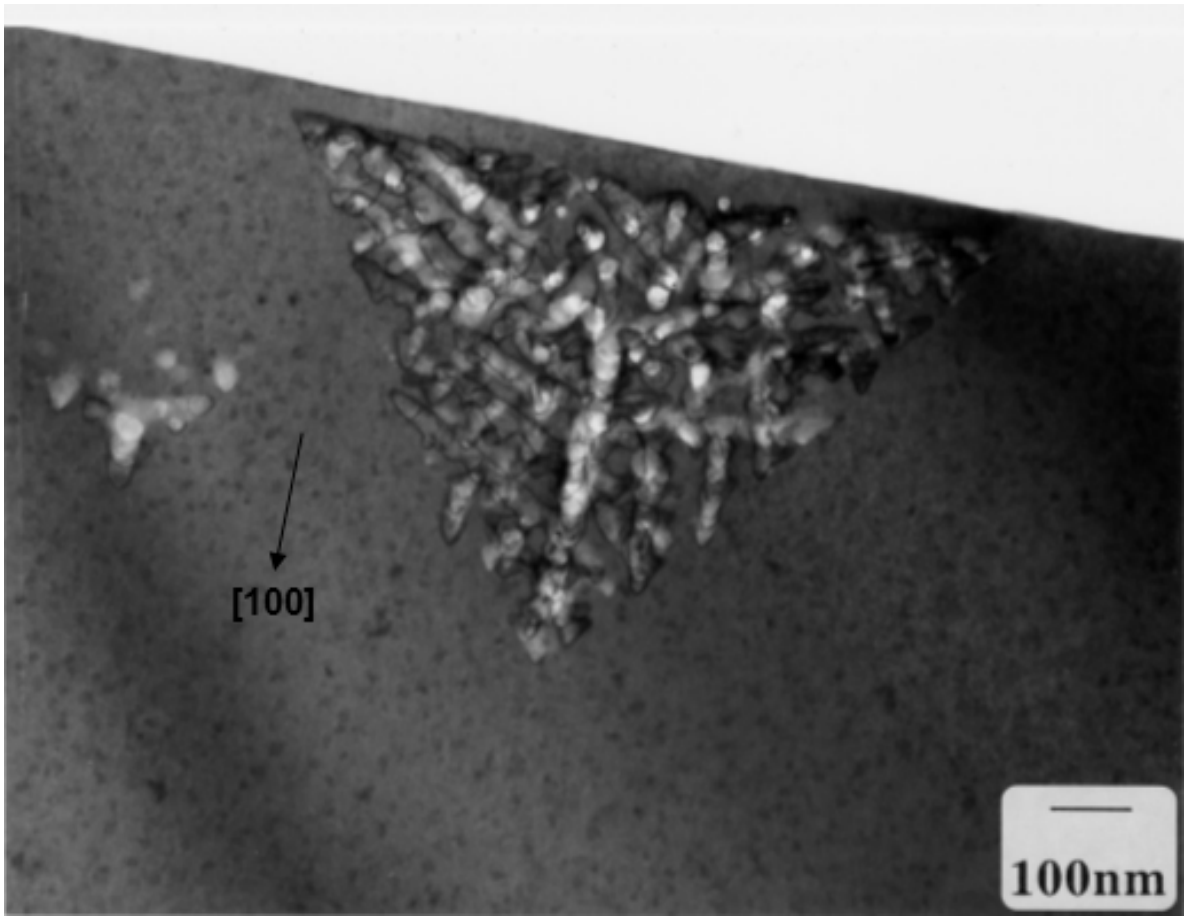

Fig. 12

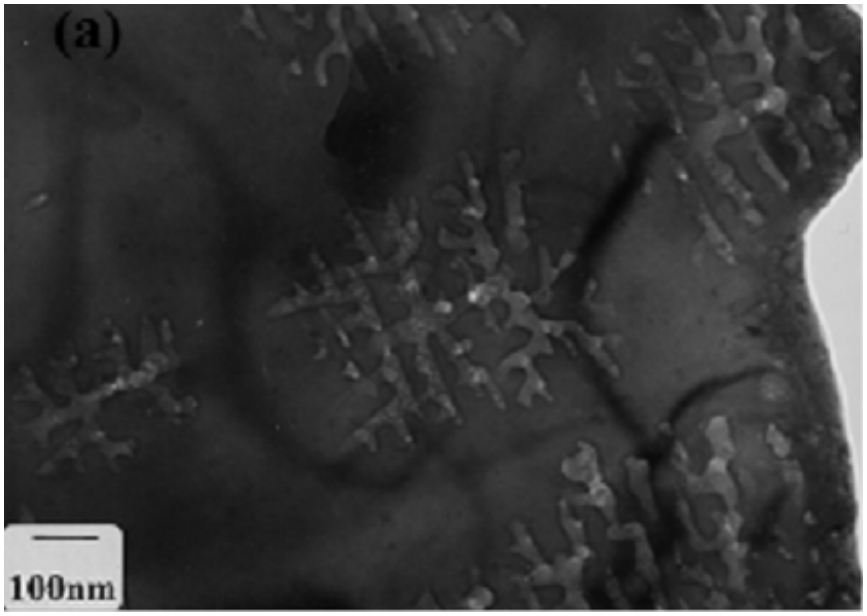

Fig. 13

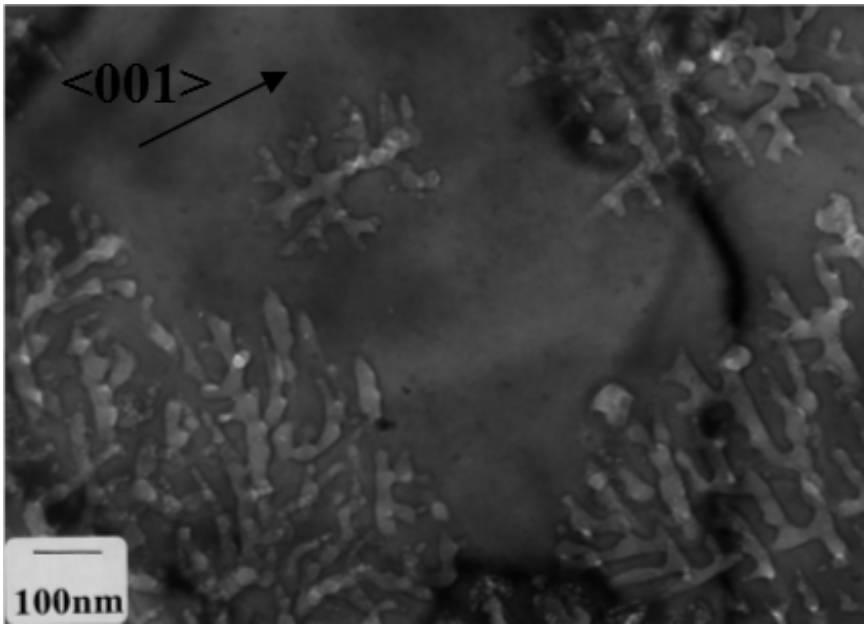

Fig. 14

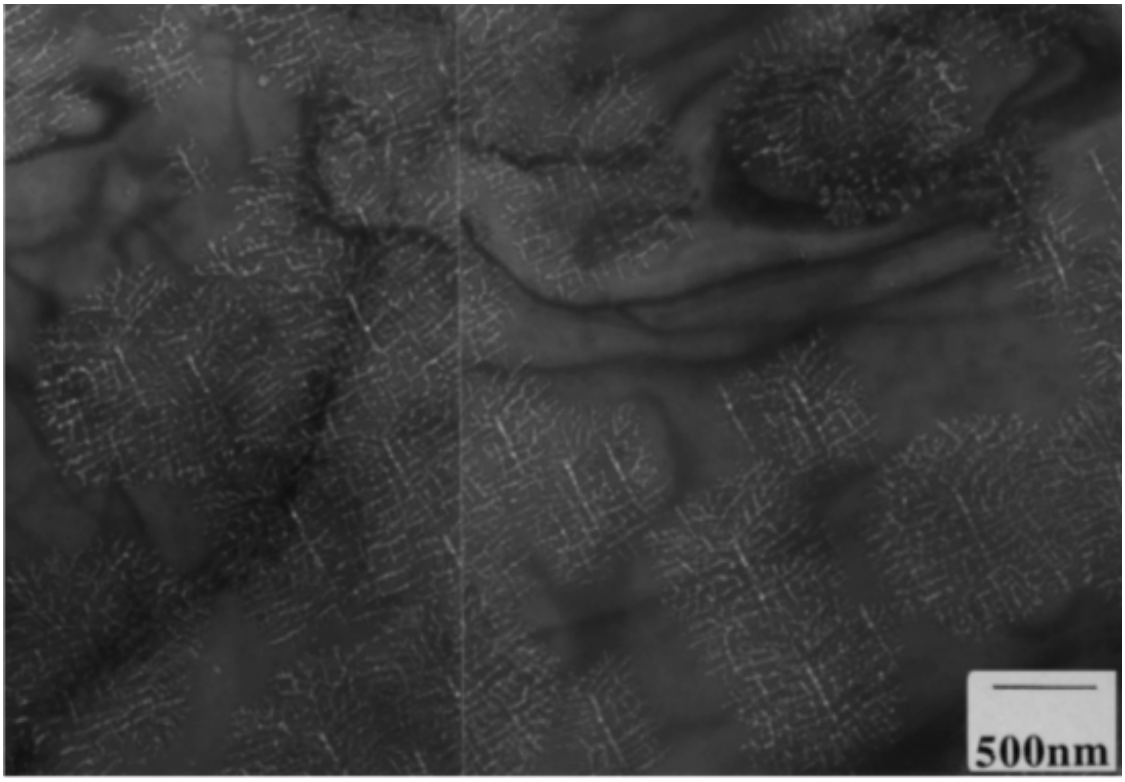

(a)

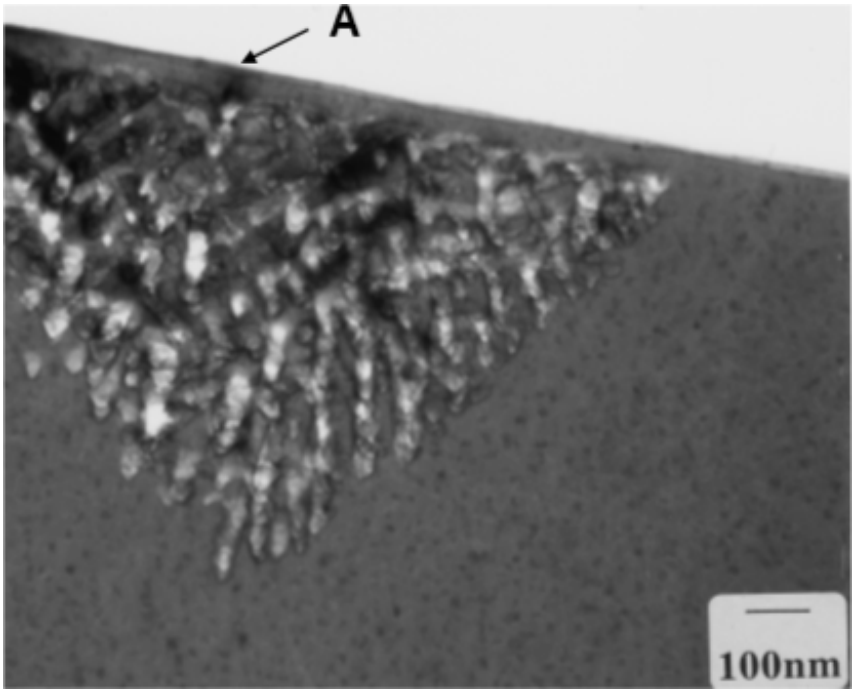

(b)

Fig. 15

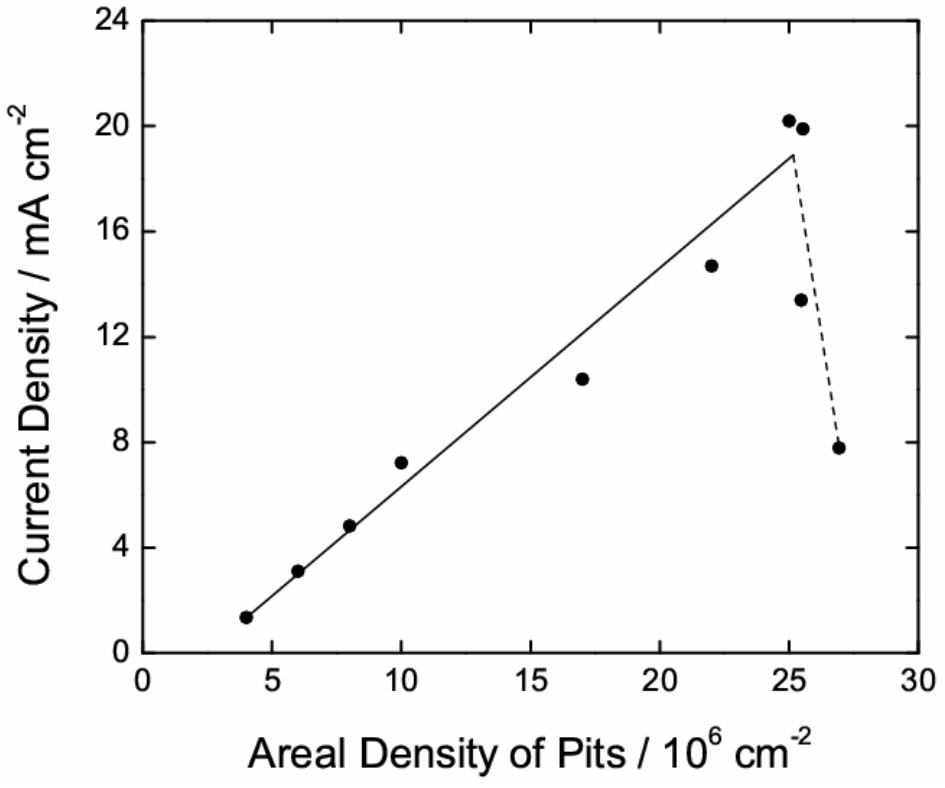
Current Density / mA cm^{-2}
Areal Density of Pits / 10^6 cm^{-2}
0
4
8
12
16
20
24
0
5
10
15
20
25
30

(a)

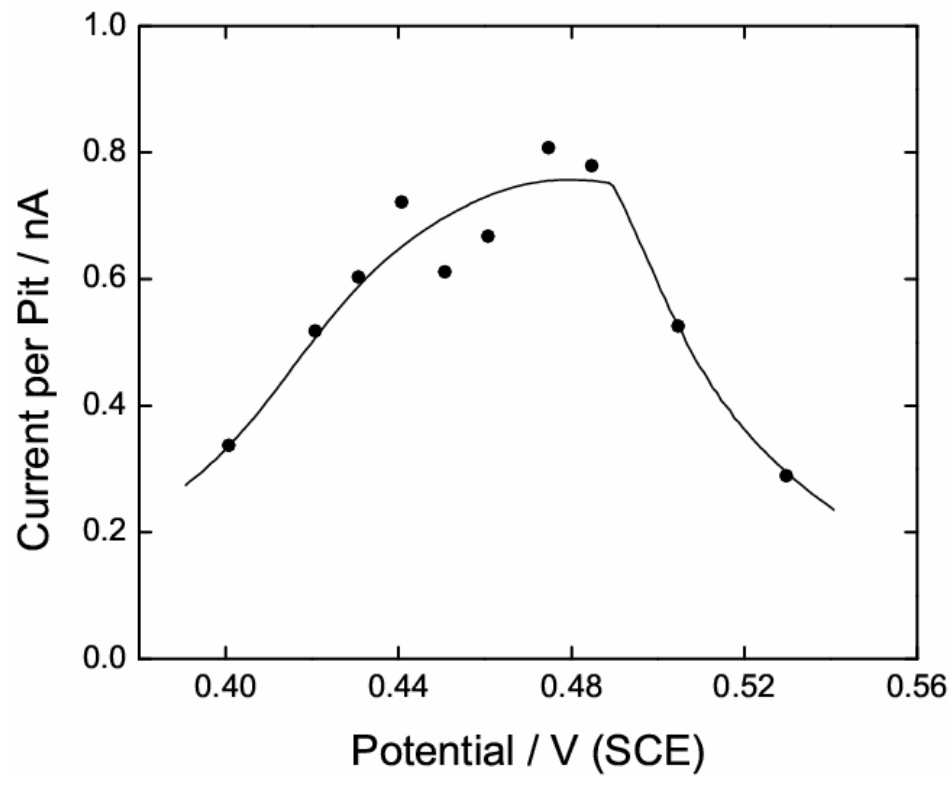
Current per Pit / nA
Potential / V (SCE)
0.0
0.2
0.4
0.6
0.8
1.0
0.40
0.44
0.48
0.52
0.56

(b)

Fig. 16

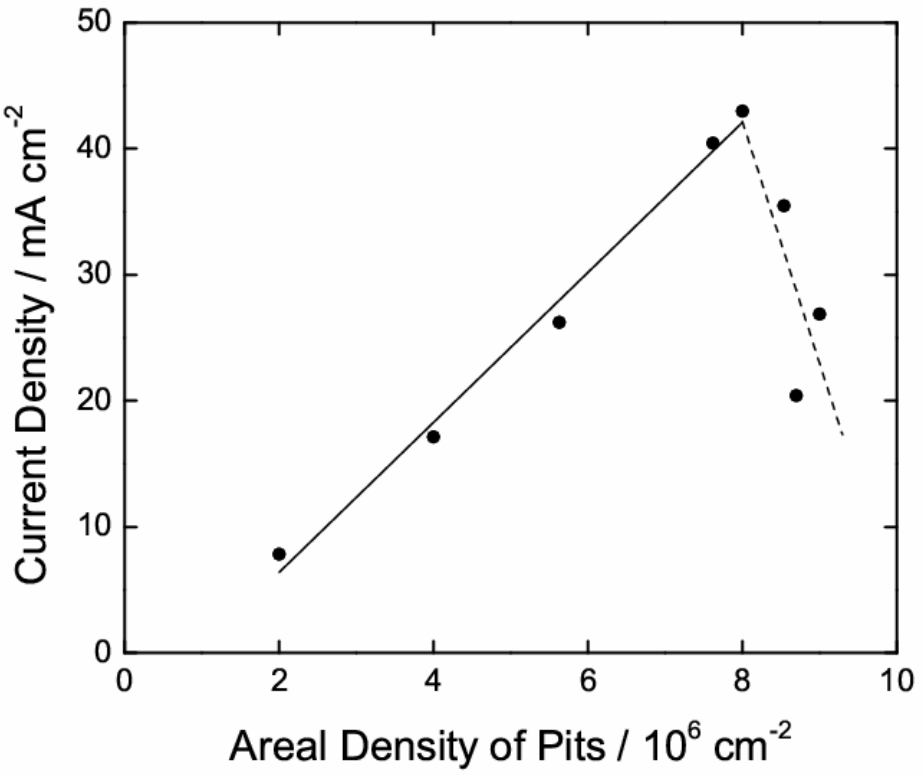
Current Density / mA cm-2
Areal Density of Pits / 10^6 cm-2
0
10
20
30
40
50
0
2
4
6
8
10

(a)

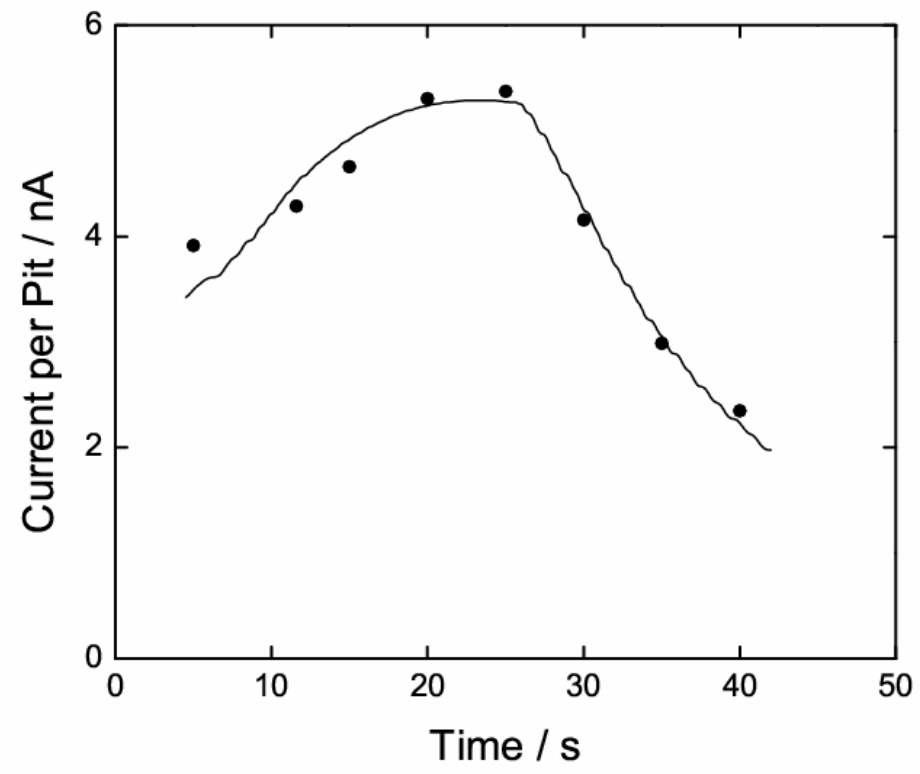
Current per Pit / nA
Time / s
0
2
4
6
0
10
20
30
40
50

(b)

Fig. 17